How to cite: *Angew. Chem. Int. Ed.* **2023,** *62,* e202303335
International Edition: doi.org/10.1002/anie.202303335
German Edition: doi.org/10.1002/ange.202303335

Fused-Ring Systems

A BN-Doped U-Shaped Heteroacene as a Molecular Floating Gate for Ambipolar Charge Trapping Memory

*Yang Yu, Le Wang, Dongqing Lin, Shammi Rana, Kunal S. Mali, Haifeng Ling,**
*Linghai Xie, Steven De Feyter, and Junzhi Liu**

Abstract: Two wide-band gap U-shaped polycyclic aromatic hydrocarbons with/without boron and nitrogen (BN-) doping (**BN-1** and **C-1**) were synthesized to tune the electronic features to suit the performance requirements for organic field-effect transistor memory (OFET-NVM). The chemical structures were characterized by scanning tunneling microscopy and single-crystal diffraction. Owing to the electron-donor effect of N and the high electron affinity of B, the **BN-1**-based OFET-NVM displays large ambipolar memory windows and an enhanced charge storage density compared to **C-1** and most reported small molecules. A novel supramolecular system formed from **BN-1** and PMMA contributes to fabricating uniform films with homogeneous microstructures, which serve as a two-in-one tunnelling dielectric and charge-trapping layer to realize long-term charge retention and reliable endurance. Our results demonstrate that both BN doping and supramolecular engineering are crucial for the charge trapping of OFET-NVM.

Introduction

Organic field-effect transistor nonvolatile memory (OFET-NVM) is a promising device with a nondestructive readout, good compatibility with complementary metal–oxide semiconductor (CMOS) circuits, low cost, and inherent design flexibility.[1] Great progress has been made, based mainly on polymer electrets and nanostructured materials as charge trapping elements (CTEs), in developing high-density and nonvolatile data storage.[2] However, the uncontrollable molecular weight and ambiguous charge trapping mechanism of polymer electrets[3] as well as the uniformity, repeatability and stability of nano-floating gates has restricted further improvements in performance.[4]

To address this problem, a ca. 1 nm molecular-floating gate (MFG) was proposed.[5] During the last decade, considerable efforts have been devoted to the design of MFGs by tailoring the molecular structures, including fullerenes,[6] acene derivatives,[7] imide derivatives,[8] and donor–acceptor small molecules.[9] An additional tunnelling dielectric layer (TDL) is generally required to act as a physical barrier for preventing the return of trapped charges. As the charge tunnelling barrier increases, however, the charge injection capacity decreases. To balance the charge injection efficiency and stable maintenance of trapped charges, hybrid CTE has been reported by doping low concentrations of MFGs into an insulating polymer matrix at the expense of charge trapping density.[9,10] However, the nonuniform distribution of aggregated MFG microdomains induced by spontaneous phase separation leads to uncontrollable film morphologies and thus poor charge trapping.[4a] Therefore, developing a novel MFG system that integrating the advantages of high charge trapping capacity and stable data retention is needed.

Polycyclic aromatic hydrocarbons (PAHs) have emerged as promising MFGs owing to their diverse chemical modifications, which have allowed for improved optoelectronic features and processability.[11] Doping heteroatoms into PAHs not only enhances their stability but also allows tuning of their optoelectronic properties and controlling their condensed behaviour in the solid state.[12] In terms of molecular design, the lone pair electrons of nitrogen (N) in heterocycles have been developed for hole trapping sites in OFET memory.[9,13] Instead of nitrogen, the boron (B) atom has an empty π-orbital, which features relatively low electronegativity and coordinative unsaturation at the trivalent B centers, leading it to be electron-deficient and serving as an electron-accepting component.[12c,14] Accordingly, incorporating B atoms into π-systems is expected to be an effective approach to accomplish high electron affinity, which can

---

[*] Dr. Y. Yu, Dr. J. Liu
Department of Chemistry and State Key Laboratory of Synthetic Chemistry, The University of Hong Kong
Hong Kong (China)
E-mail: juliu@hku.hk

L. Wang, Dr. D. Lin, Prof. H. Ling, Prof. L. Xie
State Key Laboratory of Organic Electronics and Information Displays & Institute of Advanced Materials (IAM), Nanjing University of Posts & Telecommunications
Nanjing 210023 (China)
E-mail: iamhfling@njupt.edu.cn

Dr. S. Rana, Dr. K. S. Mali, Prof. S. De Feyter
Division of Molecular Imaging and Photonics, Department of Chemistry, KU Leuven
Celestijnenlaan 200F, 3001 Leuven (Belgium)

serve as a potential electron trapping moiety in charge trapping elements but has never been reported.

Here, we report a concise and efficient method for the synthesis of a U-shaped BN-doped heteroacene (**BN-1**) for ambipolar charge trapping memory. For comparison, a pure carbon U-shaped analogue (**C-1**) was synthesized as well. The scanning tunneling microscopy (STM) study clearly reveals the U-shaped geometry and self-assembly properties at solution-solid interface for **BN-1**. The optoelectronic properties and electronic structures of compounds **BN-1** and **C-1** were systematically investigated through UV–vis absorption and photoluminescence (PL) spectroscopy and cyclic voltammetry (CV), as well as elucidated by theoretical calculations. Taking advantage of the substituent hydroxyl groups (–OH), **BN-1** was utilized as a conjugated dopant unit to develop a supramolecular-doped polymer (SDP) system,[15] which served a dual-function for charge trapping (conjugated BN-heteroacene) and tunnelling (insulating PMMA) layers.[16] Accordingly, a TDL-free OFET memory was fabricated based on pure **BN-1** and its SDP with PMMA to explore the ambipolar charge trapping behaviour and multilevel information storage. Remarkably, the resultant **BN-1** based memories demonstrated extraordinary merits with large ambipolar memory windows (52.2 V), high charge storage densities of $\approx 5.38\times10^{12}\ \mathrm{cm}^{-2}$ for hole storage and $6.25\times10^{12}\ \mathrm{cm}^{-2}$ for electron storage, 2-bit storage with 4 well-defined levels, long retention time ($>10^{4}$ s), and reliable endurance (2000 programming (P)/erasing (E) cycles), showing excellent stability and reliability compared with most reported small molecular materials (Table S4 and Figure 4e). The unprecedented observation in U-shaped BN-heteroacene suggests that the doping effect in PAHs and its SDP system play critical roles in ambipolar charge trapping and long-term memory. To the best of our knowledge, this is the first study to use BN-doped PAH as a molecular floating gate for fabricating nonvolatile OFET memory with high performance. Our work not only provides an efficient method for the synthesis of BN-doped PAH but also allows us to elucidate the role of molecular design in charge trapping OFET memory.

Results and Discussion

PAHs with a suitable energy barrier are crucial to ensure hole/electron trapping and storage stability. Ladder-type PAHs can be classified into two categories: "acenes" and "phenes", in which their electronic structures are significant difference (Scheme 1a).[17] Typically, with the same number of rings, the "phenes" have a larger energy gap than the "acenes", while the "acenes" have smaller reorganization energies than the "phenes". According to Marcus theory, a smaller intramolecular reorganization energy is favourable for charge-carrier transport.[18] Thus, the U-shaped structure enabled with a wide energy gap is aimed at enhancing charge trapping rather than charge transporting. In addition to the electronic properties, compared with the linear fused acenes, the shape of molecular configuration allows the engineering of intermolecular interactions and affects the packing model in the solid state, which are considered to be crucial factors for processability and the morphology of thin film.[19] As a result, in this work, a U-shaped BN-doped heteroacene (**BN-1**, Scheme 1b) and its pure carbon analogue (**C-1**, Scheme 1c) that possessed a high potential barrier (>3.0 eV) were designed as MFGs to trap and retain charges.

An easy-to-access, U-shaped BN-acene derivative with hydroxyl groups (–OH) and its pure-carbon analogue were synthesized in excellent yields. The precursor **P1** was synthesized by a twofold Suzuki cross-coupling with 1,3-dibromo-4,6-*N*^{4}, *N*^{6}-dihexyl benzene-diamine and *N*-hexyl-3′-(4,4,5,5-tetramethyl-1,3,2-dioxaborolan-2-yl)-[1,1′-biphenyl]-2-amine. Upon treatment of **P1** with excess boron trichloride in *o*-dichlorobenzene under reflux, the target U-shaped **BN-1** was obtained from one-shot fourfold electrophilic borylation in a 53 % yield rather than the linear NBN-doped acene derivative and other isomers (Scheme S1).[20] The -OH groups were introduced during the work-up processing due to the hydrolysis of the B–Cl bonds. Off-white powder **BN-1** showed poor solubility in small polar solvents such as toluene and dichloromethane (DCM); however, it has excellent solubility in polar solvents, including tetrahydrofuran (THF), dimethylformamide (DMF), and dimethylsulfoxide (DMSO). It is worth mentioning that the stability of **BN-1** is excellent in solution under ambient conditions, and there is no change in its NMR spectrum after six months (Figure S1). For **C-1**, the synthetic routes are shown in Scheme 1c and Scheme S2. Starting from 4,4′-((4,6-dibromo-1,3-phenylene)bis(ethyne-2,1-diyl))bis(*tert*-butylbenzene), two successive Suzuki cross-coupling with 2,2′-(2-chloro-1,3-phenylene)bis(4,4,5,5-tetramethyl-1,3,2-dioxaborolane) and phenylboronic acid gave the precursor **P2** in a total 63 % yeild. Fourfold alkyne benzannulation was achieved by treating **P2** with $InCl_3$ and $AgNTf_2$, and the resulting dechlorinated pure-carbon analogue **C-1** was obtained in a yield of 37 %. The chemical structures of compounds **BN-1** and **C-1** were unambiguously confirmed by ^{1}H-, ^{13}C-, and two-dimensional (2D) NMR spectroscopy, as well as high-resolution ESI/Maldi-tof mass spectrometry (HRMS). For further details of the synthesis and structural characterization, see the Supporting Information.

The single crystal of **C-1** was achieved from the dichloromethane solution through slowly evaporation, and further identified by X-ray crystallographic analysis (Scheme 1c, Figure S2 and Table S1.[21] The electronic structures of **BN-1** and **C-1** were analyzed by density functional theory (DFT). Figure S3 shows the optimized geometries of **BN-1** and **C-1**, which demonstrates that the U-shaped molecules have planar topological structures with a slight twist, consistent with the crystallographic analysis. The dipole moments of **BN-1** and **C-1** are calculated to be 2.47 and 0.70 Debye, respectively. The calculated frontier molecular orbitals are shown in Scheme 1d. The highest occupied molecular orbital (HOMO) energy levels of **BN-1** and **C-1** were calculated to be -5.28 and -5.40 eV, and the lowest unoccupied molecular orbital (LUMO) energy levels of **BN-1** and **C-1** were calculated to be -1.42 and -1.92 eV, respectively. In

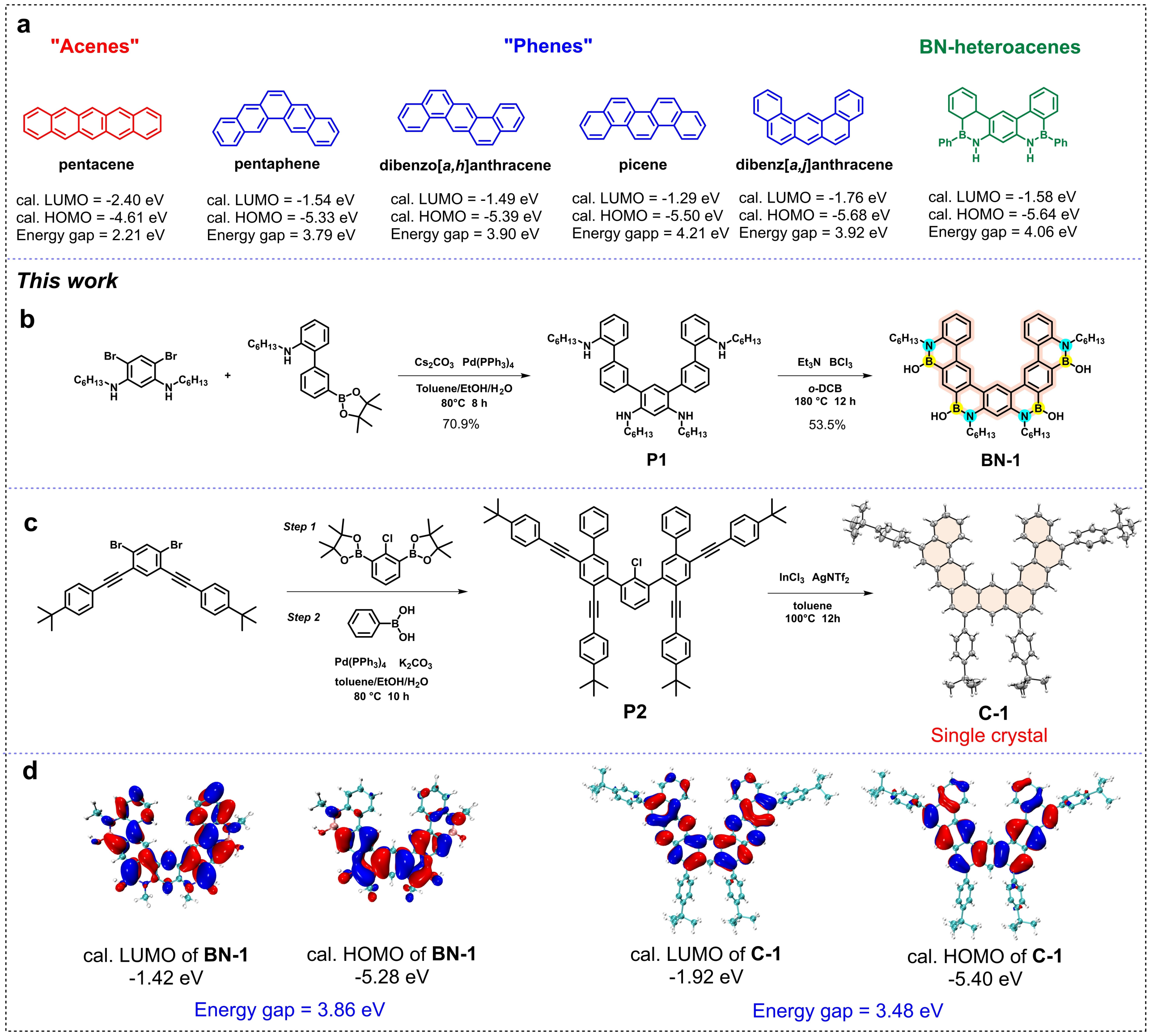

Scheme 1. a) Typical structures of ladder-type fused aromatic compounds and their calculated HOMO–LUMO levels and energy gaps. Synthetic approaches to the b) U-shaped **BN-1** and c) its pure carbon analogue (**C-1**). The single-crystal structure of **C-1** is also shown in the scheme. d) The calculated LUMOs and HOMOs of **BN-1** and **C-1**.

contrast to pure carbon analogue **C-1**, in which both the HOMO and LUMO are well distributed on the main backbone, the nonuniformly distributed HOMO and LUMO of **BN-1** can be attributed to the donor effect of N and the accepter effect of B. The results show that BN-doping in the molecular skeleton can tune the electronic structure of PAHs without significantly changing the band gap, which makes it possible to study the effect of molecular structure independently rather than band engineering in OFET memory.

The photophysical properties of **BN-1** and **C-1** were investigated by UV–vis absorption and photoluminescence (PL) analysis in both solution and films (Figure 1), and the data are summarized in Table S2. Owing to the rigid geometric structures, both **BN-1** and **C-1** exhibit two sets of absorption bands, showing electron vibronically splitting bands. In the solution, for **BN-1**, two intense high-energy absorption peaks at 282 and 298 nm with two shoulders at 317 and 328 nm and associated with two weak absorption peaks at 368 and 386 nm in the UV region, are observed. Compound **C-1** shows an intense absorption peak at 303 nm with two shoulders (289 and 316 nm), and another two absorption peaks at 366 and 387 nm with a shoulder at 350 nm in the UV region. In the thin film, the absorption bands of both **BN-1** and **C-1** were broadened and bathochromically shifted compared to those of in solution, indicating strong intermolecular interactions in the solid-state. The optical energy gaps (E_g^{opt}) of **BN-1** and **C-1** were calculated to be 3.12 eV and 3.09 eV, respectively, based on the onset optical absorption ($\lambda_{onset}^{BN-1} = 398$ nm, $\lambda_{onset}^{C-1} = 401$ nm). The fluorescence spectrum of **BN-1** exhibited a deep blue emission band with a maximum peak at 410 nm

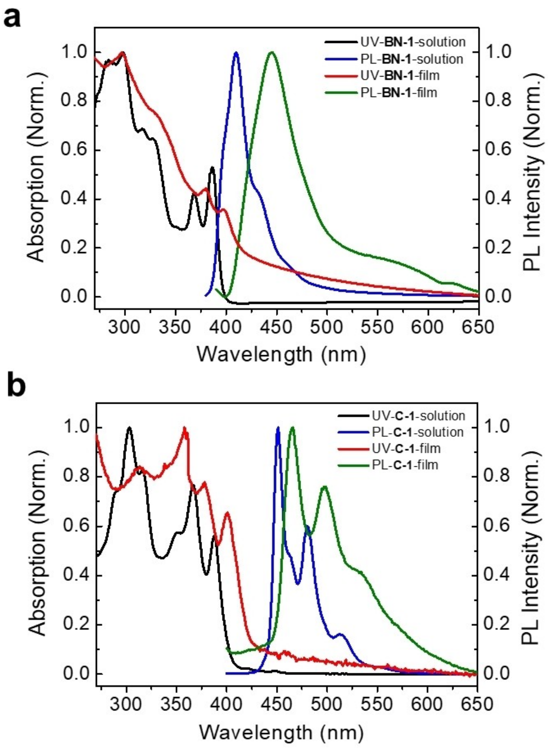

Figure 1. UV-Vis absorption and fluorescence spectra of a) **BN-1** and b) **C-1** in THF ($c = 1.0 \times 10^{-5}$ M) and in thin film.

and a shoulder peak at 434 nm. Accordingly, the Stokes shift is approximately 24 nm, suggesting a slight structural change in the excited state relative to that in the ground state. Interestingly, **BN-1** showed a small full width at half-maximum (FWHM) of 29 nm owing to its rigid molecular framework. For compound **C-1**, two narrow emission peaks at 451 to 480 nm were found in solution. Similar to the absorption spectrum, broad emission peaks with bathochromic shifts of 36 nm and 14 nm were observed in the film states of **BN-1** and **C-1**, respectively.

The electrochemical properties of **BN-1** and **C-1** were investigated by cyclic voltammetry (CV) in THF at a scan rate of 100 mV s^{-1} (Figure S4). Both **BN-1** and **C-1** exhibited irreversible oxidation. Accordingly, using the onset oxidation potential (1.06 V for **BN-1** and 1.21 V for **C-1**), the HOMO energy levels of **BN-1** and **C-1** were estimated to be −5.84 eV and −5.99, respectively. The reduction is irreversible, and no reduction wave was found within the electrochemical window. Therefore, the LUMO energy levels (−2.72 eV for **BN-1** and −2.90 eV for **C-1**) were calculated by using the equation of $E_{\text{LUMO}} = E_{\text{HOMO}} + E_{\text{g}}^{\text{opt}}$. As a result, the energy gaps of both compounds **BN-1** and **C-1** are larger than 3.0 eV, which are favourable for charge trapping in OFET memory.

The self-assembly of **BN-1** was studied at the organic solution-solid interface using STM. **BN-1** forms ordered self-assembled networks at the heptanoic acid/graphite interface and also at the 1-phenyloctane/graphite interface. Figure 2a shows a typical large-scale STM image of the self-assembled molecular network formed by **BN-1** at the heptanoic acid/graphite interface. The bright features organized in rows correspond to individual **BN-1** molecules physisorbed on the surface. The areas with darker STM contrast in between the rows are plausibly the regions where the *n*-hexyl substituents are adsorbed. The alkyl substituents were not resolved in STM images. The molecular domain to the right side of the STM image clearly reveals the U-shaped **BN-1** molecules arranged in rows. The shape of the molecules in other domains is not as apparent due to the known dependence of STM contrast on the orientation of molecular rows with respect to the fast scan axis. The network shows missing molecules defects (Figure S5). Large-scale STM images obtained at early times after deposition reveal an amorphous network which evolves into crystalline row-like arrangement as a function of time (Figure S6). In general, self-healing of the supramolecular network could be followed by recording sequential STM images in the same area (Figure S7). Figure 2b shows the smaller-scale STM image clearly revealing the row like assembly of **BN-1** molecules.

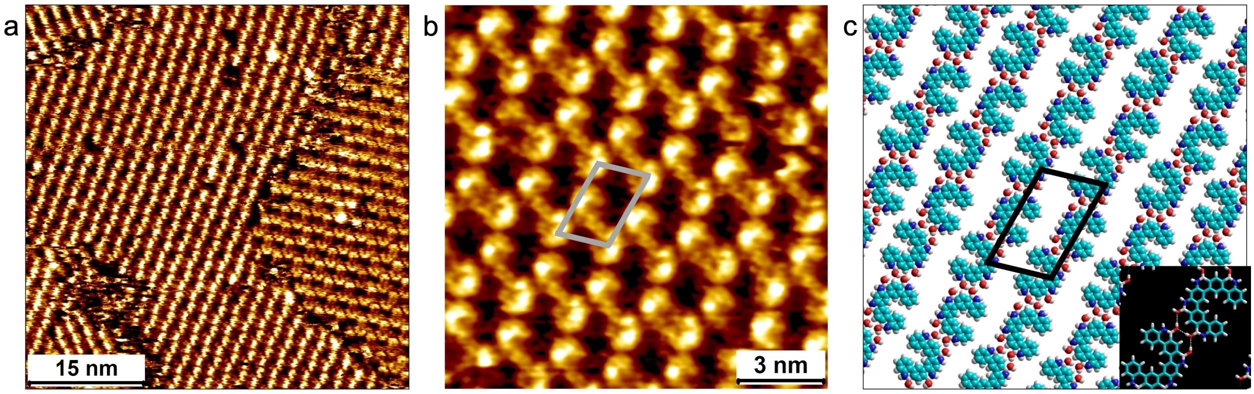

Figure 2. STM characterization of the self-assembled molecular networks formed by **BN-1** at the heptanoic acid/graphite interface. a) Large-scale STM image of the **BN-1** supramolecular network. Imaging parameters: $V_{\text{bias}} = -1.6$ V, $I_{\text{set}} = 0.14$ nA. b) Small-scale STM image. Unit cell $a = 2.8 \pm 0.2$ nm, $b = 1.9 \pm 0.2$ nm, $\gamma = 76 \pm 4°$ Imaging parameters: $V_{\text{bias}} = -1.5$ V, $I_{\text{set}} = 0.04$ nA. c) Molecular model showing the arrangement of **BN-1** molecules within the self-assembled molecular network. The inset shows the plausible hydrogen bonding pattern between adjacent molecules within a row.

Each row consists of oppositely oriented **BN-1** molecules close packed along the row axis. The unit cell parameters are $a=2.8\pm0.2$ nm, $b=1.9\pm0.2$ nm, $\gamma=76\pm4°$. A molecular model built from calibrated STM data is presented in Figure 2c which reveals that **BN-1** molecules adsorbed along the row axis possibly interact with each other via weak hydrogen bonds formed between the peripheral hydroxyl groups as indicated in the inset of Figure 2c. The peripheral *n*-hexyl chains which separate the hydrogen bonded rows along the b-vector of the unit cell are not shown in the molecular model for the sake of clarity. The results not only revealed the molecular structure of **BN-1** but also indicated the self-assembly ability for potential device application.

In MFG-OFET-NVM, one of the challenges is to reduce the volatile charge traps caused by shallow interfacial defects for hybrid CTLs, which are dependent upon the quality of the fabricated films.[22] Considering the substituted hydroxyl groups, the supramolecular BN-heteroacenes are grafted onto a nonconjugated polymethyl methacrylate (PMMA) chain via hydrogen-bond interactions (Figure 3a),[23] which allow them to be well dispersed and then contribute to generate uniform films with homogeneous microstructures and avoid phase separation between the components of **BN-1** and PMMA. ^{1}H NMR spectra provided crucial evidence for the formation of the SDP system. After introducing PMMA into the **BN-1** solution, the proton signals of the -OH groups broadened, demonstrating the formation of intermolecular hydrogen bonds[15] (Figure 3a and Figure S8). In addition, atomic force microscopy (AFM) and scanning electron microscopy (SEM) investigations supported the microscopic morphology transition from the molecular aggregate state to the SDP system. Figures 3b–3g show the AFM topographic images of pure **BN-1**, the BN-SDP system with different blend ratios (**BN-1**:PMMA = 10:1, 5:1, 1:5, 1:10) and pure PMMA-based films. The resultant films displayed average root-mean-square (RMS)

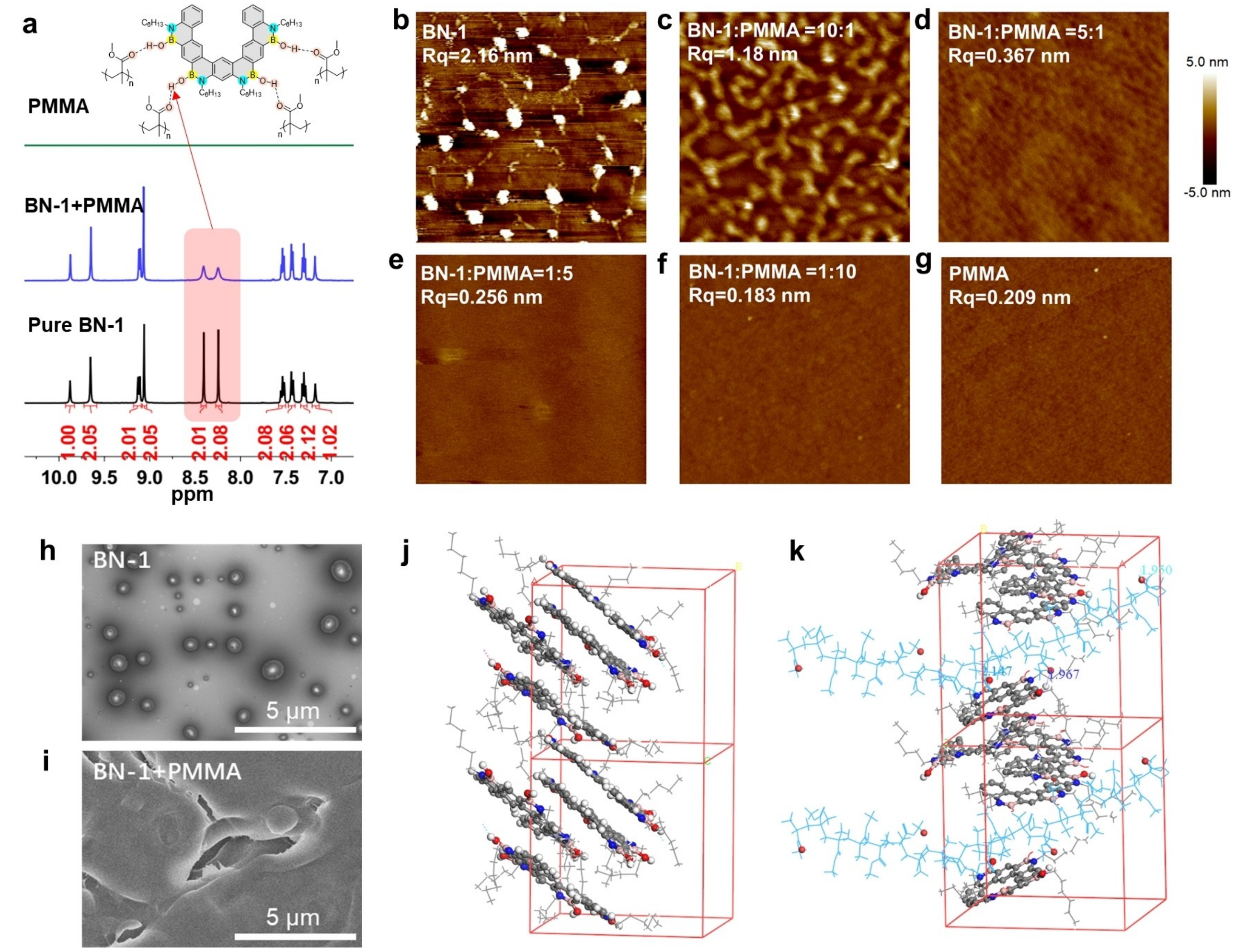

Figure 3. a) Comparation of the aromatic regions of the ^{1}H NMR spectra of PMMA, pure **BN-1**, and the mixture of **BN-1** and PMMA (1:1) in DMSO-d_6 solution. 5 μm×5 μm AFM topographic images of b) pure **BN-1**, c) **BN-1**:PMMA = 10:1, d) **BN-1**:PMMA = 5:1, e) **BN-1**:PMMA = 1:5, f) **BN-1**:PMMA = 1:10, and g) pure PMMA based films obtained by a solution spin-coating process on bare SiO_2 substrate with a RMS of 2.16 nm, 1.18 nm, 0.367 nm, 0.256 nm, 0.183 nm, and 0.209 nm, respectively. SEM image of h) pure **BN-1** film and i) the supramolecular polymer network of **BN-1** and PMMA (5:1). Molecular dynamic simulation for j) pure **BN-1** and k) the formation of hydrogen bonds between **BN-1** and PMMA in the aggregation model.

roughness values of 2.16 nm, 1.18 nm, 0.376 nm, 0.256 nm, 0.183 nm, and 0.209 nm, respectively. The pure **BN-1** film exhibited strong aggregation due to the π–π stacking and van der Waals interactions of molecules in the solid state. After blending **BN-1** with PMMA at a ratio of 10:1, the film still exhibited phase separation and high roughness. However, after improving the blend ratio to 5:1 or higher, the films obviously became flat and smooth, and the quality of morphological uniformity was even comparable to that of the pure PMMA film. From the SEM investigation (Figures 3h and i), upon the addition of PMMA to the solution of **BN-1**, a three-dimensional network structure was observed compared with the pristine aggregated pure **BN-1**, indicating the formation of the SDP system by hydrogen-bond interactions.[24] The molecular dynamic simulation evaluated the hydrogen bonds spontaneously formed with $\approx 3\,\text{kcal mol}^{-1}$ per bond between **BN-1** and PMMA (at a distance of 2.0 Å) (Figures S9 and S10). Unlike pure **BN-1** aggregates, the mixture with PMMA chains enhances the binding energy of hydrogen bonds from 3 to $10\,\text{kcal mol}^{-1}$, strengthening the mixing ability between **BN-1** and PMMA with unfavourable contributions from van der Waals forces (Figures 3j and k, and Figures S11–S14). These results suggest that the preparation of high-quality, homogeneous thin films of **BN-1** and PMMA is feasible. As a result, **BN-1** was isolated in a continuous film morphology and avoided aggregation. Accordingly, the supramolecular-doped polymer (SDP) system served as a dual-function charge trapping (conjugated BN-heteroacene) and tunnelling (insulating PMMA) layer, eliminating the unfavourable shallow defects at the interface between the transport layer and suppressing the pathway of long-term charge loss or redistribution. The naturally formed dual functional CTL could serve as a promising candidate to achieve high-performance OFET-NVM.

Figure 4a shows a schematic diagram of a pentacene-based TDL-free OFET-NVM device based on a bottom-gate top-contact configuration, consisting of a stack of 80 nm Cu source/drain electrodes, 50 nm pentacene, 70 nm single-component **BN-1** or **C-1**, or **BN-1**-SDP film (CTLs), and 90 nm SiO_2 blocking dielectric layer (BDL). All the CTLs showed hydrophobic characteristics with water contact angles of approximately 90° (Figure S15), which is beneficial for depositing pentacene with a large grain size and low trap density.[25] Figure S16 reveals the aggregation of pure **BN-1**, resulting in the formation of nanocolumn structure in the film. Compared with the smooth film of **BN-1**-SDP (5:1) and pure **C-1** based film, although rough pure **BN-1** and **BN-1**-SDP (10:1) based films limit pentacene crystalline growth, the $0.5\times0.5\,\mu\text{m}$ crystalline domains can support

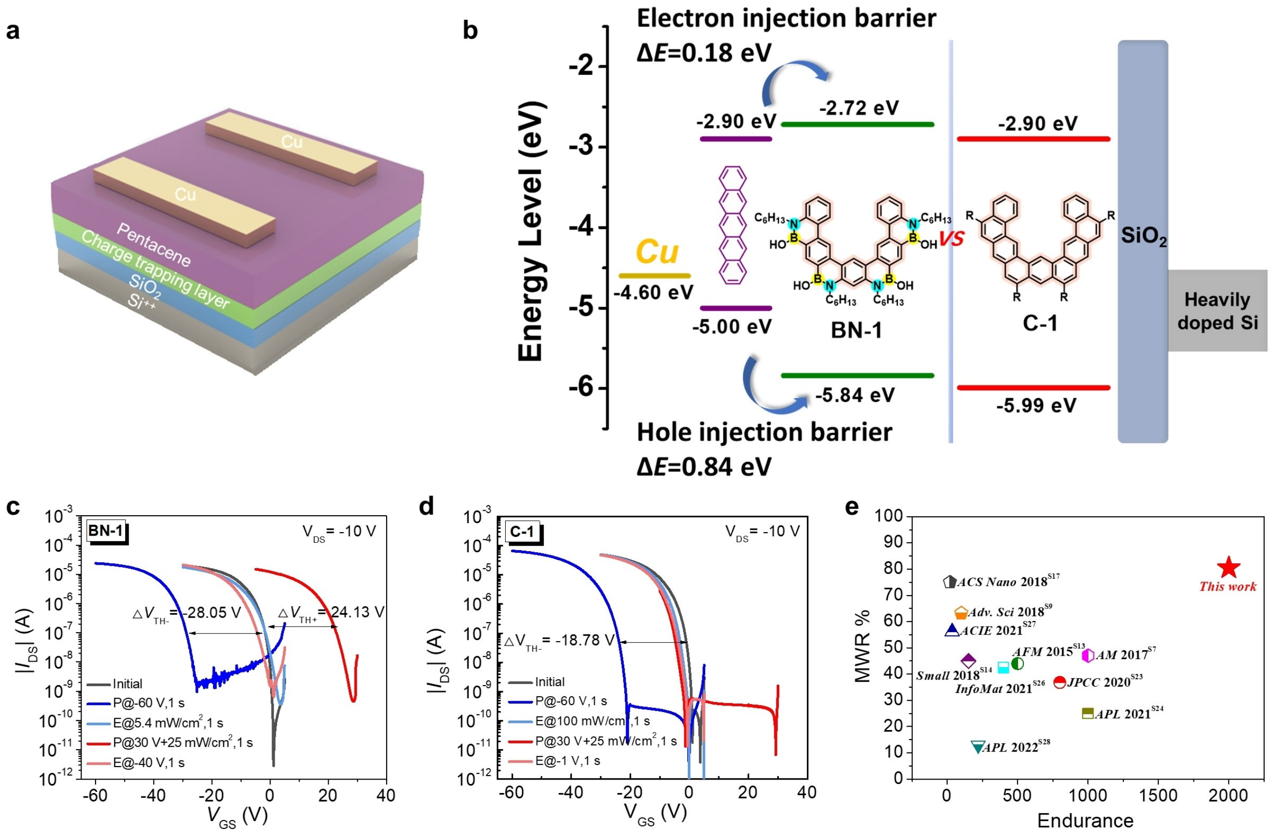

Figure 4. a) Schematic structure of the OFET-NVM device. b) Energy levels diagram of the Cu electrode, pentacene semiconductor, and MFGs, and charge trapping in the programming and erasing processes. Shifts in transfer curves for the c) pure **BN-1**- and d) pure **C-1**-based memory device. "P" and "E" represent the "programming" and "erasing" processes, respectively. e) Comprehensive comparison of the memory window ratio (MWR) and memory endurance of the proposed **BN-1**-based device with that of the state-of-art OFET memory devices reported in recent years.

good carrier injection. The appropriate energy barrier between the semiconductor channel and CTL plays a pivotal role in determining the charge tunnelling efficiency, as well as the memory window.[1c] Figure 4b shows the energy band diagram of the memory devices in the flat band state. Considering the HOMO and LUMO levels of **BN-1** and **C-1**, pentacene/MFGs have a lower electron potential height ($\Phi_{\text{w-h}} < 0.2$ eV) and a higher hole potential height ($\Phi_{\text{w-e}} >$ 0.8 eV), indicating that trapping of electrons takes precedence over trapping of holes, facilitating ambipolar charge trapping in a *p*-type semiconductor memory. The transfer and output characteristics of the **BN-1**- and **C-1**-based memory devices with these CTLs exhibit typical *p*-type field-effect behaviour (Figure S17). The well-defined linear and saturation regions of the output curves suggest a strong ability of field-effect modulation. The transfer curves of these devices show low initial threshold voltages (V_{TH}) of approximately -1 V and high ON/OFF current ratios ($I_{\text{ON}}/I_{\text{OFF}}$) ($10^5$). Compared with the pure **BN-1**-based device, the **BN-1**-SDP (5:1) based device displays large and compact pentacene grains, leading to a high mobility of 0.425 $\text{cm}^2\,\text{V}^{-1}\,\text{s}^{-1}$. However, for the pure **C-1**-based device, the transfer curve shows a high mobility of 1.73 $\text{cm}^2\,\text{V}^{-1}\,\text{s}^{-1}$ with a V_{TH} of -4.73 V and an $I_{\text{ON}}/I_{\text{OFF}}$ of 2.59×10^5. This optimal charge transport behaviour would facilitate charge injection from pentacene into the CTL.

To investigate the ambipolar charge trapping ability, the memory window (MW, ΔV_{TH}) of the devices was measured, which is defined as the difference between the V_{TH} of the programmed (P) and erased (E) states. The typical shifts in the transfer curves of the pure **BN-1**- and pure **C-1**-based devices are shown in Figures 4c and 4d. For the hole trapping mode, the writing operation was conducted by applying a negative gate bias ($V_{\text{GS}} = -60$ V for 1 s) under dark conditions; holes tunneled from pentacene and were trapped in the CTL. As a result, the transfer curves of **BN-1**- and **C-1**-based devices were shifted from their initial position towards the negative direction and then steadily sustained at that position, with a V_{TH} of -28.69 V and -23.51 V, respectively. This programming operation led to a negative shift of V_{TH} and a low conductance (OFF) state. The erasure procedure was performed by treating the devices with light illumination (power density: $W_{\text{LP}} =$ 5.4 $\text{mW}\,\text{cm}^{-2}$ for **BN-1** and 100 $\text{mW}\,\text{cm}^{-2}$ for **C-1**) for 1 s without a voltage bias. The trapped holes were neutralized by the injected photogenerated high-energy electrons, and then the transfer curves were shifted in the positive direction and recovered to their initial state, indicating a photo-reset erasing process, leading to a high conductance (ON) state. As a result, **BN-1** and **C-1** achieved hole MWs of 28.05 V and 18.78 V, respectively. The electron trapping mode was investigated by applying a programming gate bias of $V_{\text{GS}} =$ 30 V with light for 1 s, and erasing was performed by applying an appropriate negative gate bias for 1 s. Upon the programming operation, the transfer curves of the **BN-1**-based device showed a significant positive shift, suggesting an electron MW of 24.13 V. The **C-1**-based device cannot realize a $\Delta V_{\text{TH-E}}$ even under a large positive gate bias with light illumination, probably owing to the lack of electron trapping sites for the pure carbon aromatic rings, though it has almost no electron injection barriers. Table S3 summarizes the ΔV_{TH} for the hole trapping mode, electron trapping mode, and total memory window of the memories, which indicates that the pure **BN-1**-based memory shows a wider ambipolar memory window of 52.18 V than the pure **C-1**-based memory (18.78 V). It is worth mentioning that the memory window ratio (MWR, defined as the ratio of ΔV_{TH} to programming V_{GS}) of the **BN-1**-based device shows a positive MWR of 80.4%, indicating that this BN-doped heteroacene has a more substantial electron storage capability than other reported MFGs (Figure 4e and Table S4).

The charge trapping density (Δn) of the **BN-1**-based memory is calculated according to the equation $\Delta n = \Delta V_{\text{TH}}\,C_{\text{i}}/e$, where e is the elementary charge (1.602×10^{-19} C) and C_{i} is the total capacitance per unit area of the bilayer dielectrics (calculated from the equation $C_{\text{i}} = 1/C_{\text{CTL}} + 1/C_{\text{SiO}_2}$).[1c] Δn was estimated to be $5.38\times10^{12}\,\text{cm}^{-2}$ for hole storage and $6.25\times10^{12}\,\text{cm}^{-2}$ for electron storage. The results indicate that the electron donor effect of N and the high electron affinity of B contribute to an enhanced charge storage density for the PAHs, which are higher than those of the previously reported state-of-the-art small molecular CTEs (Table S4).

For π-conjugated systems, charge transfer occurs at the interface of the molecule, and the electrostatic interaction is very significant and can be described by the parameter of molecular surface electrostatic potential (ESP).[26] Accordingly, the ESP of **BN-1** and **C-1** were calculated to gain insight into the intrinsic charging property in the molecular structures (Figure S18). The minus ESP surface of **BN-1** is highly concentrated on the molecular skeleton of five undoped benzene rings and four hydroxyl groups, which is likely to generate the hole traps for positive charge stabilization. The minus ESP surface of **C-1** is delocalized on the whole aromatic skeleton. It is worth noting that the plus ESP surface of **BN-1** is prominently located between two B atoms' clip-on centre with a high potential, which simultaneously generates deep enough electron traps for negative charge stabilization.[27] An intramolecular electric field (IEF) with a direction from the B centre to the inner rings can be formed in the molecule. This IEF is conducive to driving holes towards inner rings and electrons towards the B centre, where they are trapped, facilitating stable charge storage. However, there is no obvious plus ESP surface for compound **C-1** to generate electron traps (Figure S18). Therefore, **BN-1** possesses a significant dipole moment and a non-uniform distribution of ESP, making it an excellent candidate for ambipolar charge storage. After charge trapping, the injection of holes and electrons in **BN-1** forms a radical cation and anion with one lone electron having a spin effect, respectively.[27] As shown in Figures 5a and b, the spin density distribution (SDD) contours of the ions show that the lone-electron spin density of radical cations is localized on the N atoms and the aromatic ring away from the B atoms, corresponding to the positive charge location. The spin density of the anion is mainly positioned by two B atoms and their adjacent aromatic rings. The other two charge-free B centres can further provide additional electron

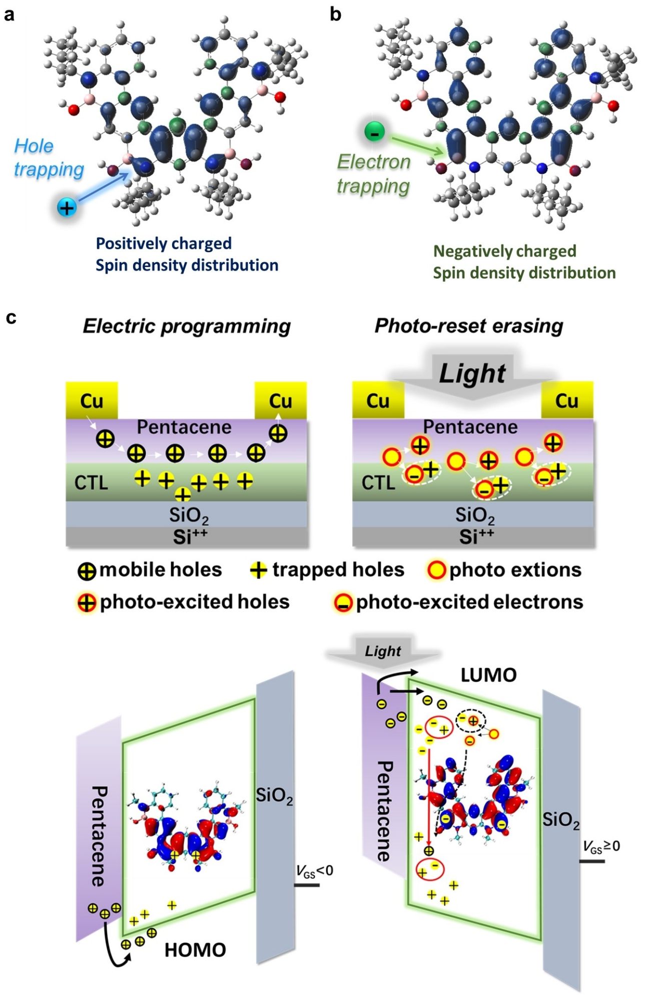

Figure 5. Spin density distributions (SDD) of a) positively and b) negatively charged **BN-1**. c) Schematic illustration of the proposed operational mechanisms and corresponding energy band diagrams of an OFET-NVM device operated in the electric programming and photo-reset erasing or photo-assistant electrical programming mode.

traps to enhance the charge storage capability. As a consequence, the N- and B-doped molecular fragments provide two independent sites for balancing the stable hole and electron trapping.

The proposed charge storage mechanism is illustrated in Figure 5c and Figure S19. Upon applying a negative gate bias, holes tunnelled from pentacene are injected into the HOMO of the molecule and then trapped by the aromatic skeleton, leading to a negative shift of V_{TH}. Although the HOMO/LUMO levels of **BN-1** and **C-1** are similar, the **BN-1**-based memory demonstrates a higher charge storage capacity, suggesting that the hole trapping ability is significantly enhanced upon the N-doping effect owing to the p–π conjugation. Namely, holes are more easily trapped on the electron-rich aromatic rings, which have a stronger negative ESP of the aromatic skeleton. When applying light illumination, as shown in Figure S20, the emission wavelength completely covered the absorption of pentacene rather than compounds **BN-1** and **C-1**; thus, the photogenerated excitons from pentacene can be separated into holes and electrons.[28] The photoexited electrons tend to accumulate at the pentacene/CTL interface and overcome the small LUMO energy barrier (<0.2 eV), finally being recombined with stored holes or quickly trapped by the B centre moieties of the molecule, resulting in the transfer curve returning to a high conductance state for photo-reset erasure or for the positive programming operation, which guarantees a broad and balanced ambipolar memory window. In the photo-reset erasing process, the **BN-1**-based device needs much weaker light intensity than the **C-1**-based device, which may be ascribed to the stronger interfacial dipole of **BN-1**, which generates an internal electric field directed from the CTL to pentacene, enhancing exciton dissociation and driving holes to transport into pentacene and electrons into the CTL.[29]

Multilevel cell (MLC) memory has become more attractive technology for consumer-grade solid-state storage because it can store more than 1 bit per cell without decreasing the cell size.[30] When applying a negative gate bias ranging from −30, −40, −50 to −60 V, the **BN-1**-based device showed a stepwise increase in the hole memory windows of 11.45, 15.28, 21.54 and 28.05 V. When applying a positive gate bias ranging from 10, 20 to 30 V, the **BN-1**-based device displayed a stepwise increase in the electron memory windows of 10.99, 17.07 and 24.05 V (Figure S21). As shown in Figures 6a and b, both $\Delta V_{TH\text{-}H}$ and $\Delta V_{TH\text{-}E}$ of the **BN-1**-based device increased linearly with enhanced negative programming bias, demonstrating finely adjustable memory states, which corresponds to the model of Fowler-Nordheim tunnelling. Owing to the linear correlation combined with the high ON/OFF drain current (I_{DS}) ratio, the **BN-1**-based memory device can function well as a multibit storage cell with four well-defined and stable current states at a reading voltage of −20 V, including one OFF state (at $V_{GS}=-60$ V), two distinct intermediate states (−50 and −40 V) and an ON state (0 V), which could be expressed as four digital states of "00", "01", "10" and "11" (Figure 6c). Namely, 2-bit data could be recorded in one single memory cell. The adjacent memory states could be well maintained and clearly distinguishable with remarkable I_{DS} ratios of greater than 10, which are superior or comparable to those of state-of-the-art small molecule based-OFET memories (Table S4).

In general, the reliability of an MLC decreases since the more levels it has would need more P/E cycles, and more levels make the read process more sensitive to noise. The endurance characteristics of the memory devices were investigated to evaluate their reliability and stability. Figure S22 illustrates the write-read-erase-read (WRER) cycling endurance characteristics measured for the pure **BN-1**-based device. For the hole trapping mode, the device exhibits reversible and reliable P/E behaviour with a distinguishable I_{ON}/I_{OFF} ratio (1.2×10^2) after 260 cycles and without any degradation. However, during subsequent harsh test conditions, the device was broken down. For the electron trapping mode, the WRER endurance was tested for 1000 cycles; the device still has an excellent I_{ON}/I_{OFF} ratio (1.9×10^2) and reversible switching behaviour. As expected,

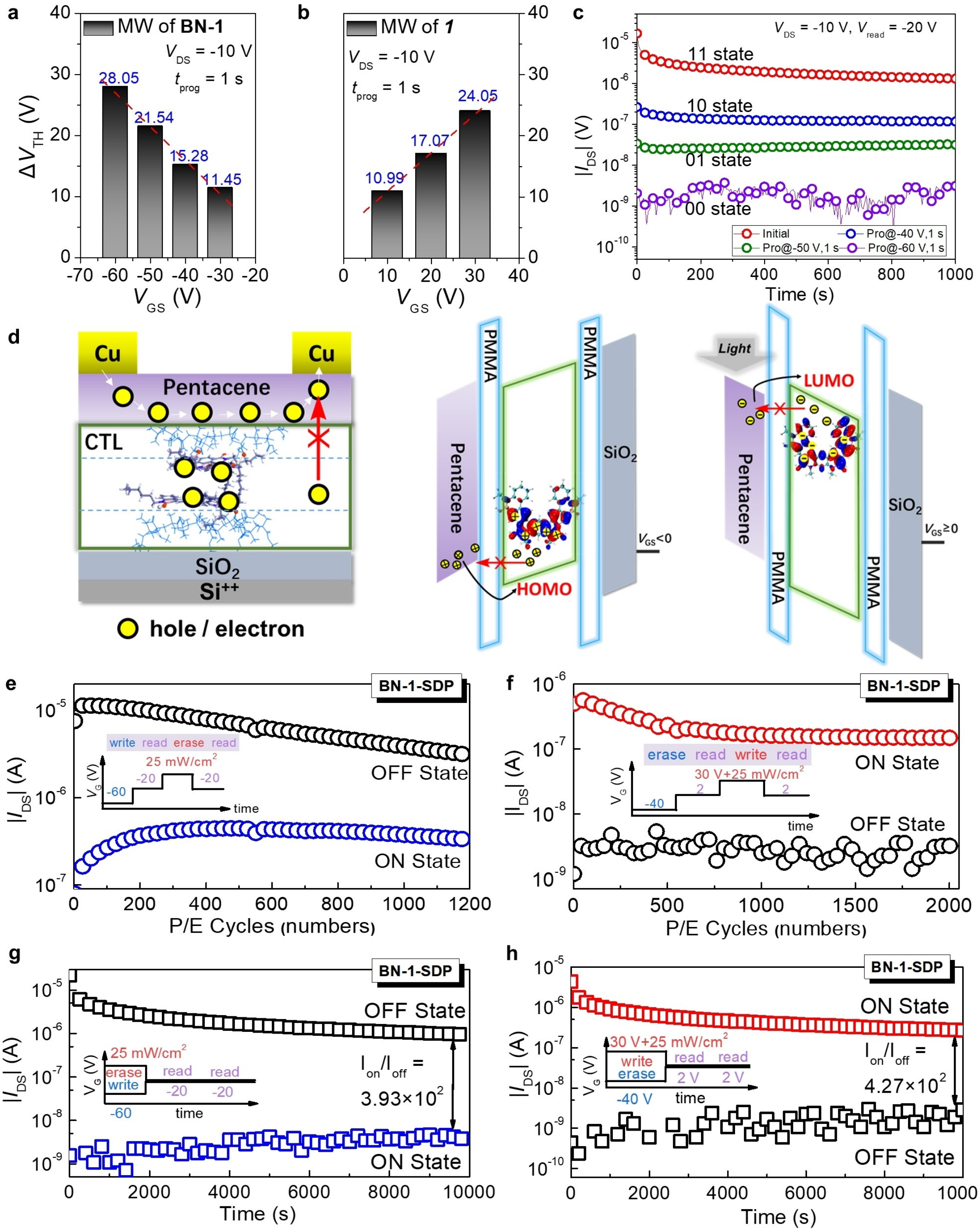

Figure 6. Memory window as a function of the programming bias of a pure **BN-1**-based memory device. a) $\Delta V_{TH\text{-}H}$ of the device was measured under the operation of various negative programming biases ($V_{GS} = -30, -40, -50, -60$ V). b) $\Delta V_{TH\text{-}E}$ of the device was measured under the operation of various positive programming biases ($V_{GS} = 10, 20, 30$ V). c) Retention characteristics of the corresponding drain currents for four state levels of the **BN-1**-based memory measured at different negative programming biases. Read at $V_{GS} = -20$ V and $V_{DS} = -10$ V. d) Illustration of the **BN-1**-SDP-based memory and charge storage mechanism. Endurance characteristics of the **BN-1**-SDP-based memory devices: e) hole trapping mode, f) electron trapping mode. Reversible switching behavior of the memory device over a series of programming, reading and erasing processes (inset). Retention characteristics of the memory devices after the writing and erasing operation maintain over 10000 s: g) hole trapping mode, h) electron trapping mode.

the endurance reliability significantly improved by the introduction of the **BN-1**-SDP system. Figure 6d shows the **BN-1**-SDP-based memory and corresponding charge storage mechanism. With a two-in-one tunnelling dielectric and charge trapping layer, the **BN-1**-SDP-based device displayed a high stable switching endurance under 1200 cycles for the hole trapping mode and 2000 cycles for the electron trapping mode, respectively (Figures 6e and f), which is the record value among the small molecule-based materials (Table S4).

Retention characteristics were also investigated to evaluate the long-term nonvolatility of memory. Figure S23 shows the retention times of the programmed and erased states in the hole and electron trapping modes, respectively. For the pure **BN-1**-based device, under hole trapping mode, both the ON state and OFF state can be well maintained for more than 10000 s without obvious degradation. However, for the electron trapping mode, the OFF state showed a decay tendency within the continuous testing, resulting in a degradation in the memory current ratio of an order of magnitude after 10000 s. In comparison, both memory states of the **BN-1**-SDP-based device can be well maintained for more than 10000 s, with a high memory current ratio of more than 10^2 without obvious degradation under two charge trapping modes (Figures 6g and h). The endurance and retention results clearly show that the **BN-1**-SDP film could contribute to maintaining reliable nonvolatile memory characteristics. Note that all the tests were conducted under atmosphere, and we believe that the optimized and packaged devices will exhibit better performance.

Conclusion

In summary, we designed and synthesized a U-shaped BN-heteroacene (**BN-1**) through a concise electrophilic aromatic borylation reaction. The STM study revealed the U-shaped geometry and self-assembly behaviour of **BN-1** at a solution-solid interface. Owing to the electron-donor effect of N and electron affinity of B, **BN-1** possesses an ambipolar charge trapping property, and the OFET memory based on **BN-1** displayed large ambipolar memory windows (52.2 V) and high charge storage density ($5.38\times10^{12}\,\mathrm{cm}^{-2}$ for hole storage and $6.25\times10^{12}\,\mathrm{cm}^{-2}$ for electron storage). In addition, a novel supramolecular system formed from **BN-1** and PMMA contributes to the fabrication of uniform films with homogeneous microstructures, which serve as a two-in-one tunnelling dielectric and charge trapping layer to realize long-term charge retention ($>10^4$ s) and P/E endurance (2000 cycles). The consistency of the theoretical analysis and experimental results supported the charge-trapping mechanism and verified the rationality of the molecular design. Accordingly, through rational molecular design, heteroatom-doping and supramolecular engineering contribute to meet the specific performance requirements of high capacity and high stability in OFET memories. Moreover, solution-processed heteroatom-doped PAHs exhibit great potential and offer a new pathway for cheap electronic devices to serve the big data and artificial intelligence era.

Acknowledgements

This work was supported by the Hong Kong Research Grants Council (27301720, 17304021), National Natural Science Foundation of China (22122114, 61905121), National Key R&D Program of China (2021YFA0717900), Natural Science Foundation of Jiangsu Province, China (No. BK20190734). S. Rana acknowledges postdoctoral fellowship from Fund of Scientific Research Flanders (FWO)-Marie Skłodowska-Curie Actions - Seal of Excellence (MSCA SOE). KSM and SDF gratefully acknowledge financial support from the FWO and KU Leuven-Internal Funds (C14/19/079). J.L. is grateful for the funding from The University of Hong Kong (HKU) and ITC to the SKL. We thank the UGC funding administered by HKU for supporting the Time-of-Flight Mass Spectrometry Facilities under the Support for Interdisciplinary Research in Chemical Science. We acknowledge the computer cluster (HPC2021) of HKU for generous allocations of compute resources.

Conflict of Interest

The authors declare no conflict of interest.

Data Availability Statement

The data that support the findings of this study are available in the Supporting Information of this article.

Keywords: Boron-Nitrogen · Charge Trapping Memory · Polycyclic Aromatic Hydrocarbon · Supramolecular-Doped Polymer

[1] a) K. Myny, *Nat. Electron.* **2018**, *1*, 30–39; b) T. Sekitani, T. Yokota, U. Zschieschang, H. Klauk, S. Bauer, K. Takeuchi, M. Takamiya, T. Sakurai, T. Someya, *Science* **2009**, *326*, 1516–1519; c) Y. Yu, Q. H. Ma, H. F. Ling, W. Li, R. L. Ju, L. Y. Bian, N. E. Shi, Y. Qian, M. D. Yi, L. H. Xie, W. Huang, *Adv. Funct. Mater.* **2019**, *29*, 1904602.

[2] a) C.-H. Kim, *Nanoscale Horiz.* **2019**, *4*, 828–839; b) Z. Zhu, Y. Guo, Y. Liu, *Mater. Chem. Front.* **2020**, *4*, 2845–2862; c) Z. Lv, Y. Wang, J. Chen, J. Wang, Y. Zhou, S. T. Han, *Chem. Rev.* **2020**, *120*, 3941–4006; d) Q. Liu, S. Gao, L. Xu, W. Yue, C. Zhang, H. Kan, Y. Li, G. Shen, *Chem. Soc. Rev.* **2022**, *51*, 3341–3379.

[3] Y. H. Chou, H. C. Chang, C. L. Liu, W. C. Chen, *Polym. Chem.* **2015**, *6*, 341–352.

[4] a) C. C. Shih, W. Y. Lee, W. C. Chen, *Mater. Horiz.* **2016**, *3*, 294–308; b) X. Chen, Y. Zhou, V. A. L. Roy, S. T. Han, *Adv. Mater.* **2018**, *30*, 1703950.

[5] S. Paydavosi, H. Abdu, G. J. Supran, V. Bulović, *IEEE Trans. Nanotechnol.* **2011**, *10*, 594–599.

[6] a) T. Xu, S. Fan, M. Cao, T. Liu, J. Su, *Appl. Phys. Lett.* **2022**, *120*, 073301; b) Q. Li, T. Li, Y. Zhang, Z. Chen, Y. Li, L. Jin, H. Zhao, J. Li, J. Yao, *J. Phys. Chem. C* **2020**, *124*, 23343–23351; c) Y. J. Jeong, D. J. Yun, S. H. Kim, J. Jang, C. E. Park, *ACS Appl. Mater. Interfaces* **2017**, *9*, 11759–11769.

[7] C. Wu, W. Wang, J. F. Song, *IEEE Electron Device Lett.* **2017**, *38*, 641–644.

[8] a) W. V. Wang, Y. Zhang, X. Y. Li, Z. Z. Chen, Z. H. Wu, L. Zhang, Z. W. Lin, H. L. Zhang, *InfoMat* **2021**, *3*, 814–822; b) Y. S. Lin, Y. C. Lin, W. C. Yang, G. S. Li, E. Ercan, C. C. Hung, W. C. Chien, W. C. Chen, *Adv. Electron. Mater.* **2022**, *8*, 2100798.

[9] Y. Yu, L. Y. Bian, J. G. Chen, Q. H. Ma, Y. X. Li, H. F. Ling, Q. Y. Feng, L. H. Xie, M. D. Yi, W. Huang, *Adv. Sci.* **2018**, *5*, 1800747.

[10] W. Wu, H. Zhang, Y. Wang, S. Ye, Y. Guo, C. Di, G. Yu, D. Zhu, Y. Liu, *Adv. Funct. Mater.* **2008**, *18*, 2593–2601.

[11] a) C. Wang, H. Dong, W. Hu, Y. Liu, D. Zhu, *Chem. Rev.* **2012**, *112*, 2208–2267; b) B. A. Hammer, K. Müllen, *Chem. Rev.* **2016**, *116*, 2103–2140; c) A. Narita, X. Y. Wang, X. Feng, K. Müllen, *Chem. Soc. Rev.* **2015**, *44*, 6616–6643.

[12] a) X. Y. Wang, X. Yao, A. Narita, K. Müllen, *Acc. Chem. Res.* **2019**, *52*, 2491–2505; b) M. Stępień, E. Gońka, M. Żyła, N. Sprutta, *Chem. Rev.* **2017**, *117*, 3479–3716; c) M. Hirai, N. Tanaka, M. Sakai, S. Yamaguchi, *Chem. Rev.* **2019**, *119*, 8291–8331; d) A. Borissov, Y. K. Maurya, L. Moshniaha, W. S. Wong, M. Zyla-Karwowska, M. Stępień, *Chem. Rev.* **2022**, *122*, 565–788.

[13] S. Seo, Y. Yoon, J. Lee, Y. Park, H. Lee, *ACS Nano* **2013**, *7*, 3607–3615.

[14] a) S. K. Mellerup, S. Wang, *Trends Chem.* **2019**, *1*, 77–89; b) Y. Min, C. Dou, D. Liu, H. Dong, J. Liu, *J. Am. Chem. Soc.* **2019**, *141*, 17015–17021; c) S. Pang, Z. Wang, X. Yuan, L. Pan, W. Deng, H. Tang, H. Wu, S. Chen, C. Duan, F. Huang, Y. Cao, *Angew. Chem. Int. Ed.* **2021**, *60*, 8813–8817; d) C. Dong, S. Deng, B. Meng, J. Liu, L. Wang, *Angew. Chem. Int. Ed.* **2021**, *60*, 16184–16190.

[15] J. Y. Lin, G. Y. Zhu, B. Liu, M. N. Yu, X. H. Wang, L. Wang, W. S. Zhu, L. H. Xie, C. X. Xu, J. P. Wang, P. N. Stavrinou, D. D. C. Bradley, W. Huang, *ACS Macro Lett.* **2016**, *5*, 967–971.

[16] Y. C. Chiang, C. C. Hung, Y. C. Lin, Y. C. Chiu, T. Isono, T. Satoh, W. C. Chen, *Adv. Mater.* **2020**, *32*, 2002638.

[17] Q. Miao, *Polycyclic Arenes and Heteroarenes: Synthesis, Properties, and Applications*, Wiley, Hoboken, **2015**.

[18] a) G. Malloci, G. Cappellini, G. Mulas, A. Mattoni, *Chem. Phys.* **2011**, *384*, 19–27; b) L. Yang, C. Z. Yin, M. A. Ali, C. Y. Dong, X. M. Xie, X. P. Wu, J. Mao, Y. X. Wang, Y. Yu, L. H. Xie, L. Y. Bian, J. M. Bao, X. Q. Ran, W. Huang, *Chin. J. Chem.* **2019**, *37*, 915–921.

[19] a) U. H. F. Bunz, J. Freudenberg, *Acc. Chem. Res.* **2019**, *52*, 1575–1587; b) Y. Li, X. Zhu, Q. Qian, C. Ma, M. Zhang, Z. Shi, J. Kuai, Y. Zhang, Z. Yan, Q. Zhang, *Adv. Intell. Syst.* **2020**, *2*, 2000155; c) Y. Wei, X. Zheng, D. Lin, H. Yuan, Z. Yin, L. Yang, Y. Yu, S. Wang, L. H. Xie, W. Huang, *J. Org. Chem.* **2019**, *84*, 10701–10709; d) N. Zhang, J. Zhu, D. An, R. Zhang, X. Lu, Y. Liu, *Org. Lett.* **2022**, *24*, 5439–5443; e) C. Li, H. Wu, T. Zhang, Y. Liang, B. Zheng, J. Xia, J. Xu, Q. Miao, *Chem* **2018**, *4*, 1416–1426.

[20] X. Wang, F. Zhang, K. S. Schellhammer, P. Machata, F. Ortmann, G. Cuniberti, Y. Fu, J. Hunger, R. Tang, A. A. Popov, R. Berger, K. Müllen, X. Feng, *J. Am. Chem. Soc.* **2016**, *138*, 11606–11615.

[21] Deposition Number 2244896 contains the supplementary crystallographic data for this paper. These data are provided free of charge by the joint Cambridge Crystallographic Data Centre and Fachinformationszentrum Karlsruhe Access Structures service.

[22] Z. L. Liu, T. P. Yu, Z. T. Wan, Y. R. Wang, Z. Q. Li, J. Yin, X. Gao, Y. D. Xia, Z. G. Liu, *Adv. Electron. Mater.* **2022**, *8*, 2101342.

[23] Y. C. Chiu, I. Otsuka, S. Halila, R. Borsali, W. C. Chen, *Adv. Funct. Mater.* **2014**, *24*, 4240–4249.

[24] a) K. W. Putz, O. C. Compton, M. J. Palmeri, S. T. Nguyen, L. C. Brinson, *Adv. Funct. Mater.* **2010**, *20*, 3322–3329; b) Y. Deng, Q. Zhang, C. Shi, R. Toyoda, D. H. Qu, H. Tian, B. L. Feringa, *Sci. Adv.* **2022**, *8*, eabk3286.

[25] C. W. Tseng, Y. T. Tao, *J. Am. Chem. Soc.* **2009**, *131*, 12441–12450.

[26] H. Yao, Y. Cui, D. Qian, C. S. Ponseca, Jr., A. Honarfar, Y. Xu, J. Xin, Z. Chen, L. Hong, B. Gao, R. Yu, Y. Zu, W. Ma, P. Chabera, T. Pullerits, A. Yartsev, F. Gao, J. Hou, *J. Am. Chem. Soc.* **2019**, *141*, 7743–7750.

[27] J. Zhang, M. Xie, Y. Xin, C. Han, L. Xie, M. Yi, H. Xu, *Angew. Chem. Int. Ed.* **2021**, *60*, 24894–24900.

[28] Y.-C. Lin, W.-C. Yang, Y.-C. Chiang, W.-C. Chen, *Small Sci.* **2022**, *2*, 2100109.

[29] a) Y. Yang, Z. Li, C. Wu, W. Li, J. Wang, M. Yi, W. Huang, *J. Mater. Chem. C* **2022**, *10*, 3292–3299; b) H. Ling, J. Lin, M. Yi, B. Liu, W. Li, Z. Lin, L. Xie, Y. Bao, F. Guo, W. Huang, *ACS Appl. Mater. Interfaces* **2016**, *8*, 18969–18977.

[30] a) T. Leydecker, M. Herder, E. Pavlica, G. Bratina, S. Hecht, E. Orgiu, P. Samorì, *Nat. Nanotechnol.* **2016**, *11*, 769–775; b) J. Y. Chen, Y. C. Chiu, Y. T. Li, C. C. Chueh, W. C. Chen, *Adv. Mater.* **2017**, *29*, 1702217.

Manuscript received: March 6, 2023
Accepted manuscript online: March 25, 2023
Version of record online: April 25, 2023